Control of antisolvent mass transfer through porous membranes for the crystallization of organic compounds

Sara Chergaoui[1,2], Damien P. Debecker[2,3], Tom Leyssens[2,3], Patricia Luis[1,2*]*

[1] Institute of Mechanics, Materials and Civil Engineering - Materials & Process Engineering (iMMC-IMAP), Université catholique de Louvain (UCLouvain), Place Sainte Barbe, 2 bte L5.02.02-B, 1348 Louvain-la-Neuve, Belgium
[2] Research & Innovation Centre for Process Engineering (ReCIPE), Université catholique de Louvain (UCLouvain), Place Sainte Barbe, 2 bte L5.02.02-B, 1348 Louvain-la-Neuve, Belgium
[3] Institute of Condensed Matter and Nanosciences (IMCN), Université catholique de Louvain (UCLouvain), Place Louis Pasteur, 1 bte L4.01.06, 1348 Louvain-la-Neuve, Belgium

Abstract

Crystallization faces great challenges from the point of view of technology readiness, process economics, and energy consumption. Membranes are capable of controlling both energy and mass transfer and they can lead to major improvements if integrated into antisolvent crystallization processes. For example, limiting unfavorable kinetics and thermodynamics that are responsible for undesired crystal size and shape. In this work, membrane-assisted antisolvent crystallization (MAAC) was used to crystallize the amino acid L-serine. Two commercial membranes made of polyvinylidene fluoride (PVDF) and polypropylene (PP) with water contact angles of 130° and 150° respectively, allowed a controlled antisolvent crystallization. These membranes controlled the transmembrane mass transfer of antisolvent (ethanol) under different feed and antisolvent velocities at ambient conditions. In all cases, a narrow crystal size distribution (CSD) of L-serine was obtained reflected in a coefficient of variation (CV) of 31-37%, compared with batch antisolvent crystallization or drop-by-drop crystallization where the CV was 63 and 54% respectively. Thanks to the measurement of L-serine and ethanol concentration along the operating time, the mass transfer coefficient of MAAC was evaluated. Increasing the antisolvent or the crystallizing solution velocity showed that a too high value of one or the other could result in wetting or system blockage (inside the membrane contactor, module, or tubing). This study explains the transmembrane mass transfer in MAAC and the resulting crystal properties.

Keywords: Antisolvent crystallization; membrane contactor; hydrophobic membranes; L-serine; process intensification.

Synopsis

Membrane-assisted antisolvent crystallization (MAAC) is investigated through the evaluation of the transmembrane mass transfer, the evolution of supersaturation and its impact on crystal size and size distribution. L-serine in water was chosen as the crystallization system with ethanol as antisolvent. Some potential challenges in MAAC operation were also addressed and their mitigation pathways.

Graphical abstract

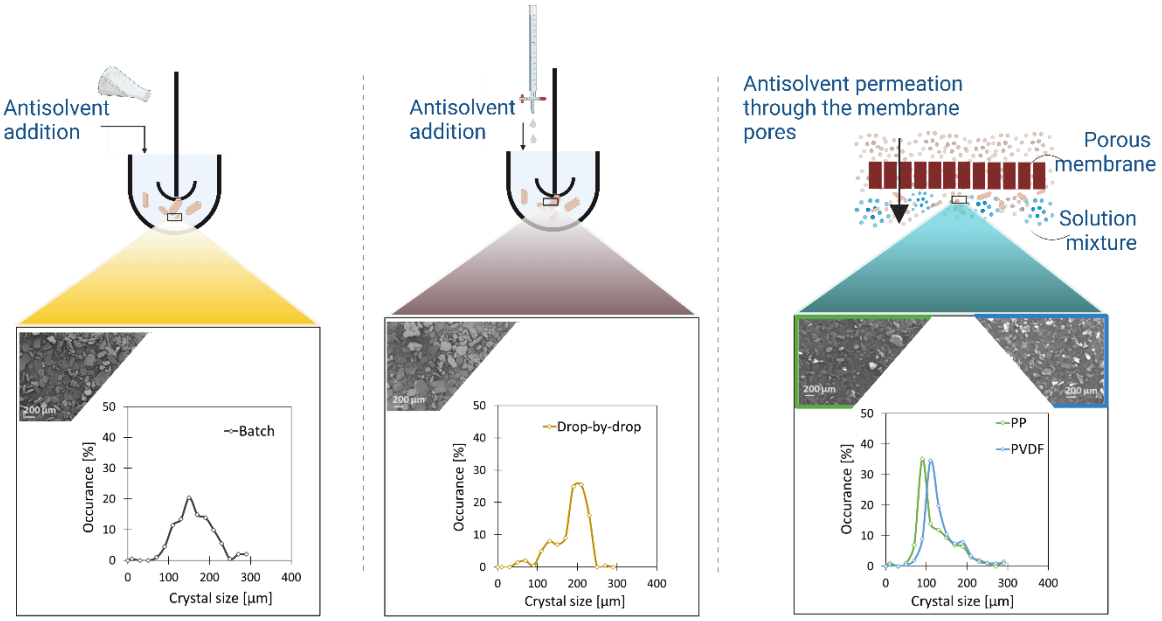

1. Introduction

Tremendous progress in control of solution crystallization processes was made since the 1990s thanks to: (a) in situ real-time sensor technologies such as attenuated total reflection-Fourier transform infrared (ATR-FTIR) spectrometry and laser backscattering probes that could provide much richer data sets suitable for crystallization modeling; (b) faster computers and control hardware, which enabled the application of population balance modeling and the implementation of advanced techniques for systems control; and (c) increased interest in manufacturing drug crystals of higher consistency and quality.[1–3] The control of solution crystallization process implies supersaturation control and ideally monitoring of the crystal size distribution.[4]

The median crystal size obtained in a crystallization process depends on the nucleation rate and the crystal growth kinetics, both of which increase strongly with supersaturation.[5] Local levels of supersaturation depend on mixing, and the risk to spontaneously nucleate around the antisolvent addition point in the crystallizer is inevitable. This is even more pronounced with large stream inlets (10 - 20 mm in diameter), for which a significant amount of time may be needed to get sufficient solution mixing. Local high supersaturations may lead to precipitation of non-uniform material. To remediate this issue, antisolvent can be added at a lower temperature after an initial seeded cooling process (Figure 1).[6,7] This allows less solute remaining in the solvent and a much higher surface area of crystals available to consume the generated supersaturation.[8] Another alternative is the use of a pipe crystallizer with a mixing unit, such as the impinging jet mixer, T or a Y mixer.[9] Both of these solutions do not, however, provide an intensified process, they remain batch-based, as opposed to membrane-assisted crystallization, which has emerged recently as a technology to control different crystallization processes.[10]

Membrane-assisted antisolvent crystallization is a novel approach that combines effective mixing and accurate control of antisolvent mass transfer, avoiding unfavorable local supersaturations. Advantages

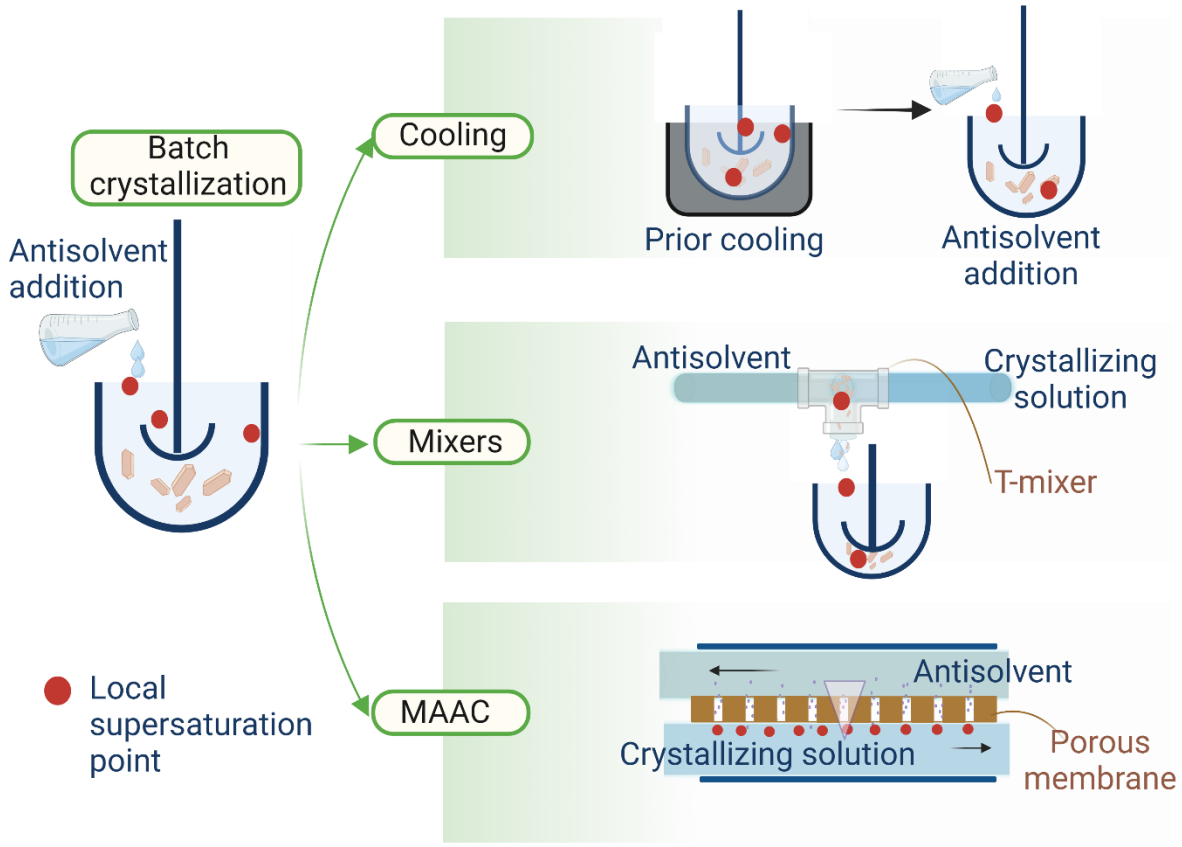

Figure 1: Cooling and the use of mixers prior to antisolvent are some approaches attempted to avoid high local supersaturation when adding the antisolvent to the crystallizing solution.

of utilizing MAAC are: (i) It controls the mass transfer of the antisolvent into the crystallizing solution, via tuning operating conditions and appropriate membrane properties;[11] (ii) It provides homogeneous mixing given first the numerous entry points of the antisolvent through the membrane pores; second, the variation of the crystallizing solution hydrodynamics according to flow rates and membrane module;[12] (iii) MAAC can be fine-tuned to different applications in agro- and pharma- industries.[13] Membrane material can differ to match environments of different pH, temperature, with a wide pore range and thicknesses; and (iv) It is a promising solution to process intensification integrating other process functions besides crystallization such as reaction purification.[14] MAAC nonetheless, is yet to overcome some limitations to its efficient application: (i) membrane pore clogging can occur depending on the interactions between the solute and membrane surface;[15] (ii) different membrane modules exist on the market, but only flat-sheet and hollow-fiber ones have been explored so far, so spiral-wound or tubular membrane modules are yet to be explored to facilitate their application; (iii) the transmembrane mass transfer is not yet understood nor its correlation with resulting crystal properties.

MAAC uses the concentration or the activity difference between the two sides of the membrane as the driving force of the mass transfer (Figure 2).[11,13] The membrane acts as a physical barrier between the crystallizing solution and the antisolvent.[16] The mass transfer of the antisolvent through the membrane is a crucial factor that distinguishes MAAC from conventional processes. MAAC is a relatively new membrane-based technology, and few studies have been reported so far. Each study expresses the impact of MAAC on crystal properties by evaluating the antisolvent transmembrane mass transfer and/or the crystal shape, size and distribution (CSD). Di Profio *et al.*, described the antisolvent transmembrane mass transfer in function of temperature and concentration.[17] Tuo *et al.*, attributed the transport of the

antisolvent to the pressure difference between the tube and shell side of the hollow-fiber membrane module and showed this transport could be controlled by modifying the solutions velocity. It was explained that the speed at tube and shell sides can maintain a stable driving force.[18] Sheng *et al.*, showed how the antisolvent permeation forms a layer at the shell side due to the concentration difference between the liquid layer at the membrane surface and crystallizing solution. No compound was crystallized for this demonstration, as the focus was on the transfer of the antisolvent.[11]

Fern *et al.*, used computational fluid dynamics (CFD) to illustrate the mixing effect under different membrane pore sizes, and crystallizing solution flow rates. The antisolvent flow rate in all experiments was kept constant and at values higher than that of the crystallizing solution. The study showed that membrane pores allowed for the formation of numerous mixing interfaces that promoted macromixing, forming narrow CSD.[19] Zarkadas *et al.*, showed that crystallization occurring at the shell side of the membrane module was more successful than that of the tube side, where arguably some pore or tube blockage took place. The longer residence time at lower crystallizing solution speed resulted in better mixing and crystal properties.[12] Chen *et al.*, showed the possibility of developing coated drug particles using MAAC and they tackled variations of tube and shell side velocities, which resulted in different particle sizes. The study demonstrated that higher antisolvent speed is better for a higher supersaturation and mixing at the membrane surface, producing drug particles of smaller size than the initial (as-received) drug. The resulting drug particles had the same molecular structure and coating thicknesses.[20] Finally, Li *et al.*, showed that under a certain antisolvent addition rate prolonged crystal growth region could be used for constructing an ideal and uniform crystal morphology.[16]

Even though the success of MAAC in tailoring the crystal properties of different organic compounds is highlighted by the above examples, the relation between the antisolvent mass transfer through the membrane and the crystal properties has not yet been studied. The abovementioned studies, limit to either the mass transfer evaluation or to the study of crystal properties.[11,17,20,21] Furthermore, they do not agree on the mass transfer evaluation either linking it to the concentration,[16] or the pressure difference.[18] In this study, we take a systematic approach to the evaluation of the antisolvent mass transfer using the

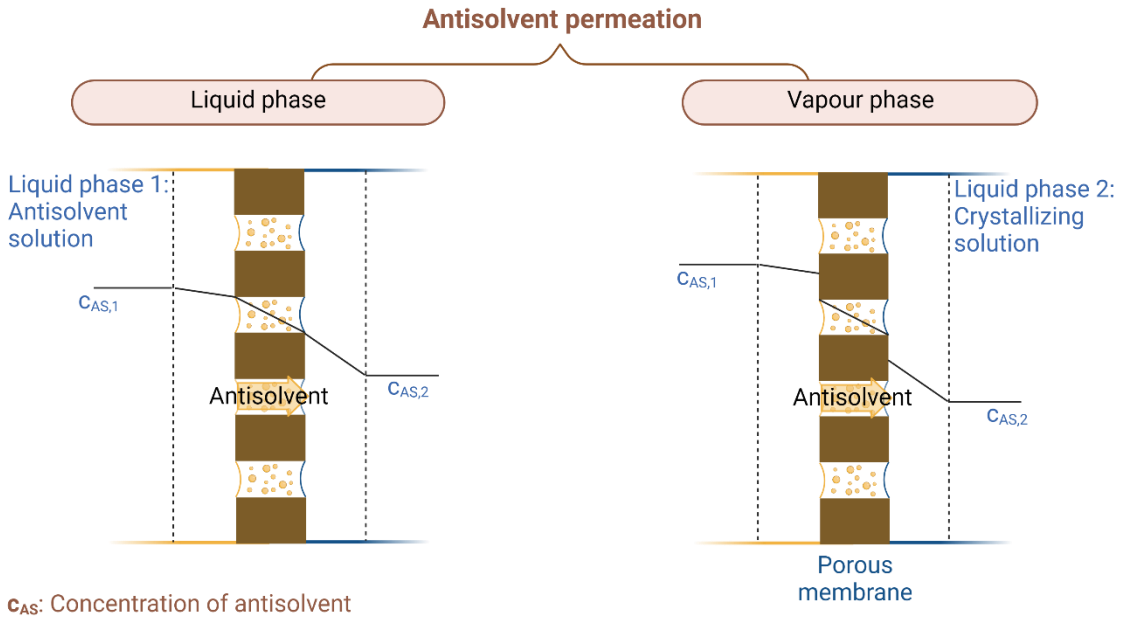

Figure 2: Demonstration of the concentration profile of the antisolvent through the porous polymeric membrane during MAAC operation. Depending on membrane and antisolvent properties, the latter can either permeate in the vapour phase in the absence of wetting, or the liquid phase otherwise.

transmembrane flux and most importantly the mass transfer coefficient. Furthermore, we evaluate the crystal properties and supersaturation evolution in a quest of correlating between the transmembrane antisolvent mass transfer to the resulting crystal properties.

2. Materials and methods

2.1. Material

Polypropylene (PP) flat sheet membranes were purchased from 3M GmbH (Germany), while Polyvinylidene fluoride (PVDF) membranes were purchased from Merck Chemicals (Belgium). Both PP and PVDF membranes are hydrophobic with water contact angle of 150° and 130° respectively, possess a sponge-like cross-sectional structure and have a pore size of c.a. 0.2 µm. L-Serine was purchased from Sigma-Aldrich (Belgium) and used as received. The rest of chemicals used in this study are listed in Table 1.

Table 1: The list of chemicals used in the course of this study.

Chemical	Characteristics	Supplier (Belgium)
Ultrapure Water	18.2 MΩcm	Lab
L-serine	**Purity:** ≥99 %	Sigma-Aldrich
Absolute Ethanol	**Purity:** ≥99.5%	VWR Chemicals
Acetonitrile	**Purity:** ≥99.95 %	VWR Chemicals
Methanol	**Purity:** ≥99.8 %	VWR Chemicals
Norvaline	**Purity:** ≥99.0 %	Sigma-Aldrich
3-Mercaptopropionic acid	**Purity:** ≥99.0 %	Sigma-Aldrich
Orthophosphoric acid 85%	**Purity:** 85.6 %	VWR Chemicals
FMOC Chloride	**Purity:** ≥99.0 %	Sigma-Aldrich
Phthaldialdehyde	**Purity:** ≥99.0 %	Sigma-Aldrich

2.2. Membrane performance in MAAC

The experimental set-up (Figure 3 and Figure S1) was built to evaluate the performance of membranes in conducting antisolvent crystallization. The crystallizing solution containing L-serine (solute) and ultrapure water (solvent) is directed by a gear pump (Cole Parmer, Belgium) at a specific flow rate, to the bottom cell of the membrane module. The antisolvent was circulated at the upper cell of the membrane module using a gear pump (Verder, Belgium) as well. The core of the setup is the membrane module that was purchased from DeltaE Srl (Italy) and had a membrane effective surface of 12×10 cm. Each experiment was run at least twice. The analytical balance (VWR, Belgium) allowed for the continuous tracking of the mass variation of the antisolvent as it permeated through the membrane pores to the crystallizing bulk solution.

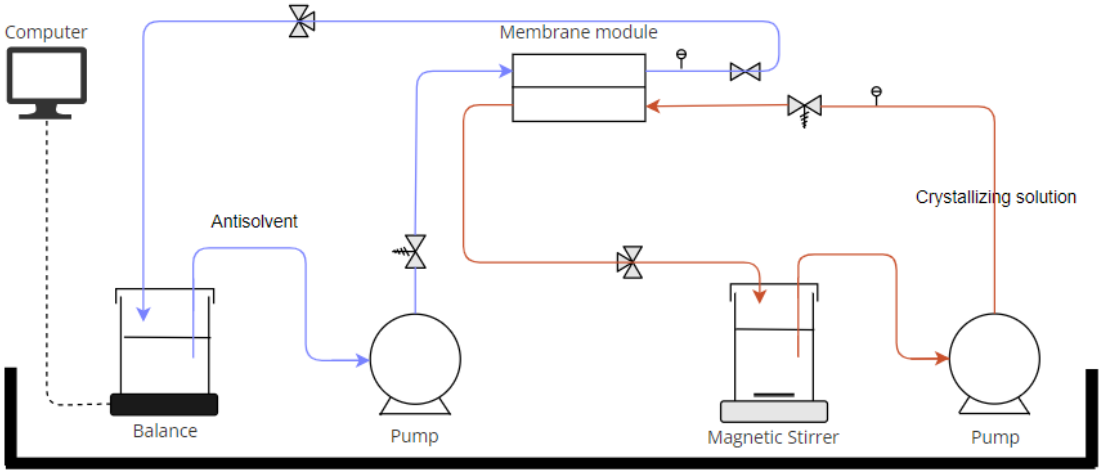

Figure 3: Experimental setup. The crystallizing solution is directed by a gear pump at the selected flow rate, to the bottom cell of the membrane module. Likewise, the anti-solvent is circulated using a gear pump at the chosen flow rate at the upper cell of the membrane module. As the anti-solvent permeates through the membrane contactor, the mass decreases which is tracked by the balance that is connected to the computer for data collection.

As for the batch and drop-by-drop experiments, they were conducted under identical operating conditions as with MAAC, i.e., same stirring rate of the bulk solution of 380 rpm, same temperature (20 °C), same initial crystallizing solution concentration (26 wt.% L-serine) and same final ethanol concentration in the liquid solution (20 wt.%). Crystals from batch crystallization appeared immediately, while it took around 90 seconds with drop-by-drop and at least 30-40 minutes with MAAC.

Antisolvent transmembrane flux

The antisolvent mass transfer flux was calculated using the weight difference of the antisolvent with time in the crystallizing solution, considering the weight fraction of ethanol detected by GC, and the total mass of the crystallizing solution at time t_i:

$$J = \frac{1}{A}\frac{w_{as}(t_i) - w_{as}(t_{i+1})}{t_i - t_{i+1}} \qquad \text{(Eq. 1)}$$

With J being the antisolvent transmembrane flux in kg/ m^2.s, A the active membrane area (0.012 m^2), w_{as} the weight of the antisolvent in kg and t_i the operation time in s.

The overall mass transfer coefficient K (kg/m^2.s) was then calculated using the equation:

$$J = K.\frac{\left(a_f(t_i) - a_{as}(t_i)\right) - \left(a_f(t_{i+1}) - a_{as}(t_{i+1})\right)}{\ln\left(\frac{\left(a_f(t_i) - a_{as}(t_i)\right)}{\left(a_f(t_{i+1}) - a_{as}(t_{i+1})\right)}\right)} \qquad \text{(Eq. 2)}$$

With a_f and a_{as} are the ethanol activity coefficients ($a = x.\Upsilon$) in the feed and antisolvent solutions, respectively, which were obtained from the UNIFAC thermodynamic model for water/ethanol at incremental mass fractions of ethanol from 0 to 1. Aspen Plus was used to perform the calculations of activities (Figure S2). To ensure no water permeates through the membrane pores, water is kept at atmospheric pressure, which is lower than the liquid entry pressure (LEP). The latter is the pressure at which the liquid permeates through the membrane pore and is measured according to Equation 3:[22]

$$LEP = -\frac{2\,\gamma_L}{r_p}\,cos\alpha \qquad \text{(Eq. 3)}$$

With γ_L the liquid surface tension in N/m, α the contact angle in degree and r_p the pore radius in m. For water, LEP values were 12.4 and 7.2 bars through PP and PVDF membranes respectively.

High Pressure Liquid Chromatography (HPLC)

L-serine was quantitatively measured in both the crystallizing bulk solution and the antisolvent solution at 5, 10, 20, 40 and 75 min of the experimental operation time, using the HPLC equipped with a Shim-pack GIST C18 column (Shimadzu, Belgium). 0.5 g of bulk solution samples were first diluted with 800 g of water. Then, 1 g of the diluted solution was added to 1g of 4 mM Norvaline standard solution. A similar approach was followed for the sampled retrieved from the antisolvent solutions, but with the addition of 200 g of water only as traces or no L-serine is expected in these samples. The calibration curve employed for HPLC chromatogram interpretation is given in Figure S3.

Gas Chromatography (GC)

The ethanol content was quantified for samples at 5, 10, 20, 40 and 75 min of the experimental operation time using a Thermo Scientific™ - TRACE 1300 Gas Chromatograph equipped with a flame ionization detector (FID). Samples were retrieved from both the crystallizing solution side and the antisolvent side. The former allows to determine the ethanol content in the solution, and hence estimate the supersaturation creation, while the latter allows detecting potential wetting. 0.5 g of the retrieved sample is then mixed with 0.5 g of 0.01 wt.% Acetonitrile solution. The GC analysis was run at least twice for each sample. The calibration curve employed for GC analysis interpretation is shown in Figure S4.

Supersaturation

In antisolvent crystallization, the driving force for the process is created by mixing a solution with an antisolvent, and can be expressed as $\Delta\mu = kT \ln S$. The supersaturation ratio is defined as $S = c/c^*$ (unitless), with c being the actual concentration in solution and c* being the equilibrium concentration in solution.[23]

2.3. Membrane characterization

Membrane morphology

Scanning Electron Microscope (SEM) (Zeiss, ULTRA with Bruker EDS chemical analyzer) was employed to portray the morphology of the membranes. Membranes were beforehand immersed into liquid nitrogen for a clean cross-sectional cut. Next, a thin layer of gold was deposited under vacuum with a sputter coater (Quorum Q150 RS) to make the samples conductive.

Membrane hydrophobicity

The hydrophobicity of the membranes was measured using the Optical Contact Angle (OCA) (DataPhysics OCA20). Three measurements were taken for each membrane sample using sessile drop method with 5 µL droplet of water.

Membrane surface

The presence of functional groups at the membrane surface was assessed via Fourier-transform infrared spectroscopy (FTIR) using Thermo Scientific Nicolet iN10. FTIR spectrum is recorded between 4000 and 400 cm^{-1}.

2.4. Solubility curve determination and characterization of crystals

Solubility

Water/ ethanol mixtures were prepared with ethanol concentrations of 0, 20, 40, 60 and 100 wt.%, and were mixed with an excess of L-serine. The solutions were stirred at room temperature (20 °C) for 12 hrs before filtration under vacuum. The filtered solution was dried for 72 hours and the weight of the samples was measured every 24 hrs, until the weight stopped differing. The resulting weights were used to determine the solubility of L-serine (Figure S5).

Crystal shape

Crystals were recovered both from the membrane surface and the bulk crystallizing solution at the end of each experiment. They were dried under the fume hood overnight. A thin layer of gold was deposited under vacuum with a sputter coater (Quorum Q150 RS) for conductivity before SEM imaging.

Crystalline form

To evaluate the crystal form of L-serine crystals, powder samples evaluated using X-ray diffraction (XRD, Bruker D8 Advance, Cu Kα radiation, λ=1.5406 Å) in the range from 2theta = 10 to 100 degree.

Crystal size distribution

The particle size distribution was analyzed using ImageJ analysis of SEM images of the resulting L-serine crystals from both bulk solution and membrane surface.

3. Results and discussion

3.1. Antisolvent mass transfer

The antisolvent flux through the membrane and, particularly, the mass transfer coefficient, have barely been reported in literature. It is important though to study the mass transfer of the antisolvent to understand the kinetics that are necessary to control crystal-related phenomena. Herein, the progress of the transmembrane flux and the mass transport coefficient throughout MAAC operation is quantified. Two cases were considered for the study of each membrane: one where the antisolvent solution is fixed to 1.7×10^{-4} $m.s^{-1}$ while the crystallizing solution varying from 1.7, 2.5 to finally 3.3×10^{-4} $m.s^{-1}$; the second case was the other way around, i.e., the crystallizing solution was kept fixed. This way, the impact of the solution velocity either from the feed or the antisolvent side of the membrane can be evaluated. Stability of the transmembrane flux can be hindered either due to the fluid's density, pore blockage, possible impregnation of crystals inside the membrane matrix, or blockage in the fittings or membrane module. By observation, blockage happened mostly inside the tubes, and the membrane cell, so the accumulation of crystals began at the tubing or inlet walls and ended in complete blockage as the concentration of crystals increased.

Based on the antisolvent transmembrane flux (Figure 4), one observes:

i) For either PP or PVDF membrane, the flux takes about 20 minutes stabilizes to a value that is $\leq 5 \times 10^{-3}$ $Kg.m^{-2}.s^{-1}$. The same tendency was observed by Tuo *et al.*,[18] studying the transmembrane flux of ethanol in polyethersulfone hollow fiber membranes and by K. Sirkar *et al.*[12] studying 2-propanol in polypropelene hollow fiber membranes. This feature is common in most membrane processes.[24] The flux followed a two-step evolution as illustrated in Figure 4-a: (I) an initial decline phase, and (II) steady state period. This can be attributed to the appearance of the first nuclei within the first 20 minutes of

operation, then the solution stabilizes resulting in a steadier permeation of the antisolvent. At optimized solution flow rates, i.e., in the case where the antisolvent solution was set to 2.5 $\times 10^{-4}$ m.s^{-1}, while the crystallizing solution was at 1.7 $\times 10^{-4}$ m.s^{-1}, samples were retrieved from the crystallizing solution every 10 minutes from their first appearance (Figure S6). With increase of antisolvent concentration in the crystallizing solution, the crystal size increased from 26 to 110 µm on average. The crystal morphology evolved from hexagonal plates at initial appearance in solution to an orthorhombic morphology by the end of experiment. The metastable zone width increases with increasing antisolvent permeation rate in accordance with supersaturation generation rate.[17] Membranes provide a higher permeation flux at the beginning of the operation (phase I, Figure 4), then the flux stabilizes (Phase II, Figure 4). This implies that supersaturation rate increases faster in the first phase than in the second. This variation in supersaturation rate eventually impacts the evolution of crystal shape observed in Figure S6.

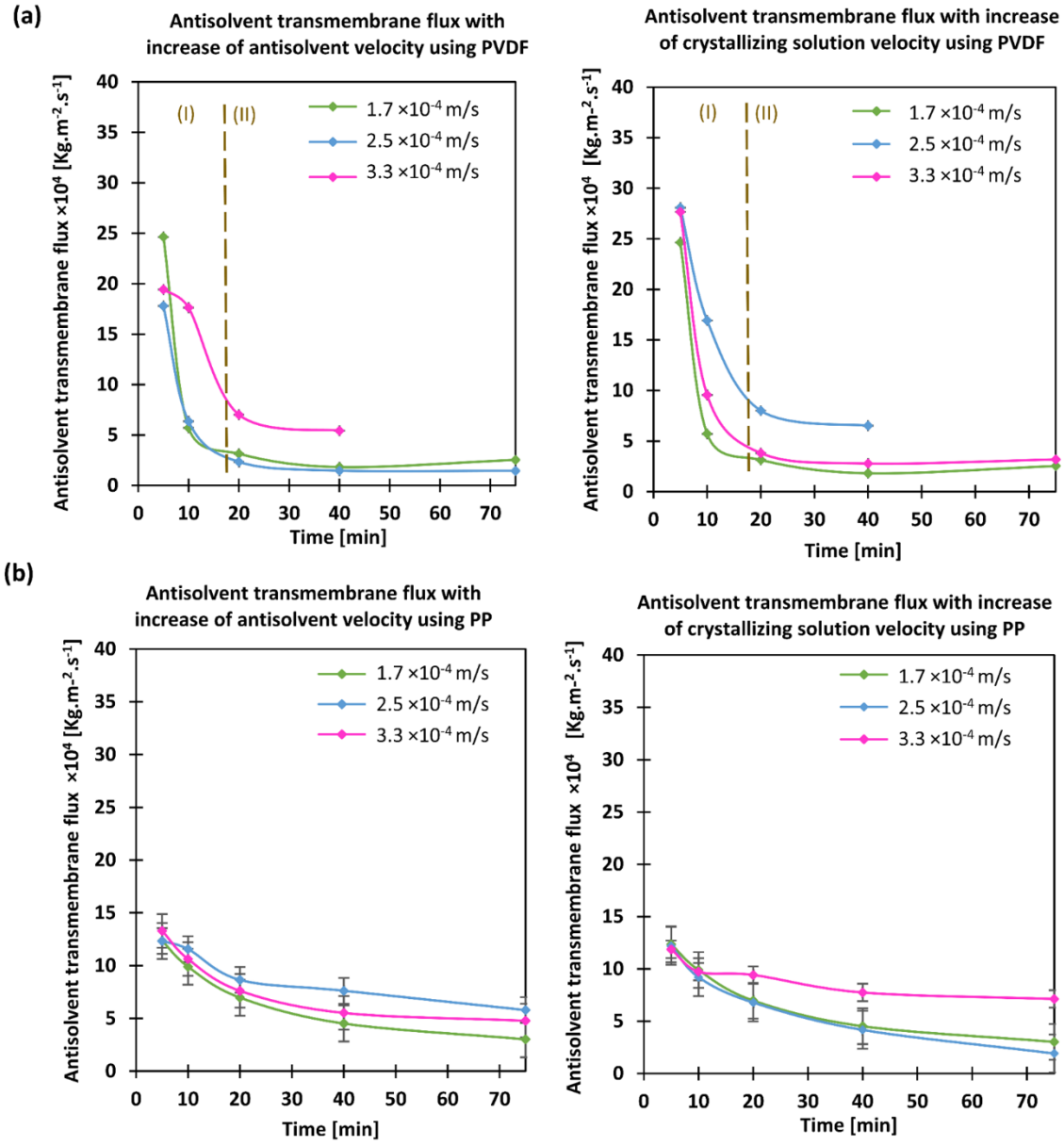

Figure 4: Antisolvent transmembrane flux through (a) PVDF and (b) PP membranes during MAAC operation. The antisolvent velocity was from 1.7 to 3.3 $\times 10^{-4}$ m.s^{-1}, while fixing the crystallizing solution at 1.7 $\times 10^{-4}$ m.s^{-1} (left plots). The crystallizing solution velocity was also varied from 1.7 to 3.3 $\times 10^{-4}$ m.s^{-1}, while fixing the antisolvent at 1.7 $\times 10^{-4}$ m.s^{-1} (right plots). The lines are used as a guide to the eye. Each experiment was run at least twice.

ii) MAAC operations lasted 75 minutes at all conditions with PP membranes before reaching blockage, which originated mostly in the membrane module or alternatively at the tubing wall due to the deposition of crystals, resulting in a limited flow of the crystallizing solution. This phenomenon was more apparent for PVDF membranes where blockage took place at about 40 minutes under two conditions (Figure 4-a).

iii) Overall, the flux resulting from PVDF membranes was lower than that of PP membranes. This likely stems from the different affinity the antisolvent (ethanol) has towards the two membrane polymers. Ethanol has higher affinity towards PVDF than PP given the Flory-Huggins parameter $\chi_{ethanol\text{-}PVDF}$= 1.61 and $\chi_{ethanol\text{-}PP}$= 4.4 for PVDF and PP respectively,[25,26] so the latter could exhibit less attractive forces at the walls of membrane pores during the permeation of the ethanol molecules.

iv) As for the impact of either the crystallizing or the antisolvent solution velocity, the crystallizing solution resulted in an increase of the antisolvent transmembrane flux at 2.5 $\times 10^{-4}$ m/s with both PVDF and PP membranes, then a slight decrease at 3.3 $\times 10^{-4}$ m/s, with respect to the first case where both solutions were set at 1.7 $\times 10^{-4}$ m/s. When the crystallizing solution flows faster, the higher turbulence delays crystal growth, so the crystals appear later during the experimental operation time, avoiding possible blockage membrane pores that can reduce the transmembrane flux (Figure 5). On the other hand, when the crystallizing solution flows even faster, the pressure inside the membrane module at the feed side increases, so the membrane liquid entry pressure in some pores can be partially surpassed causing some molecules from the liquid solution to permeate through the membrane to the antisolvent side (Figure S7). This reverse flux can be responsible for the slight decrease of the antisolvent

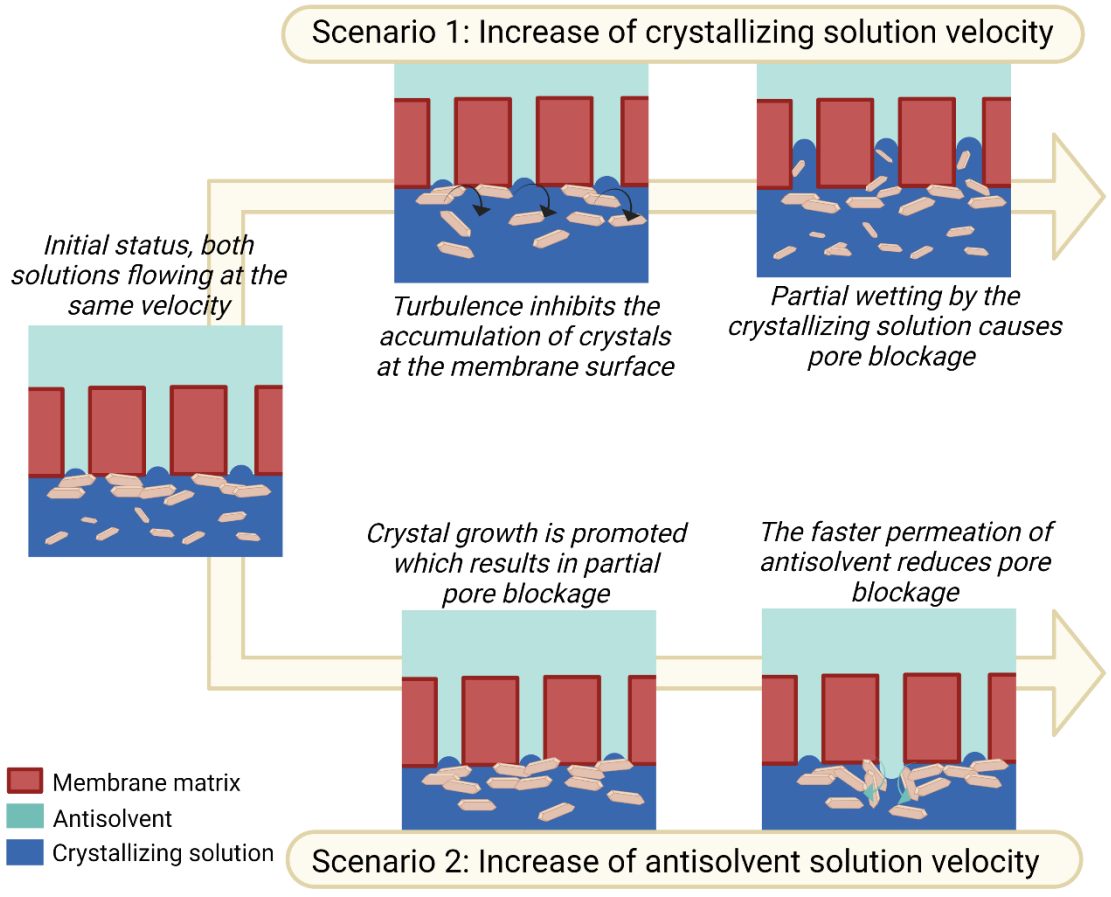

Figure 5: Illustration of the impact of crystallizing and antisolvent solution velocities. For a best control of the antisolvent transmembrane flux, no pore wetting is to happen from either solution which corresponds to the case where antisolvent solution is set at 2.5 $\times 10^{-4}$ m.s^{-1} and the crystallizing solution is set at 1.7 $\times 10^{-4}$ m.s^{-1}.

transmembrane flux. With the increase of antisolvent solution velocity, a slight decrease of the antisolvent transmembrane flux at 2.5 $\times 10^{-4}$ m.s^{-1} takes place, in this case the shear forces result in less antisolvent permeating through the membrane pores, promoting as well crystal growth rather than nucleation, which produces larger crystals at the membrane surface that cause further resistance to the mass transfer. When the flow rate increases even further to 3.3 $\times 10^{-4}$ m.s^{-1}, an increase of the transmembrane flux was observed, which is due to the higher pressure at the membrane module in the antisolvent side, pushing it through the pores even faster, which also washes off any crystals that could be attached at the vicinity of the pores.

The evolution of the mass transfer coefficient with time remained stable in optimum cases, slightly more stable with PP membranes compared to PVDF (Figure 6). The correlation between the solutions' velocity from either side of the membrane, and the antisolvent mass transfer is complex involving the

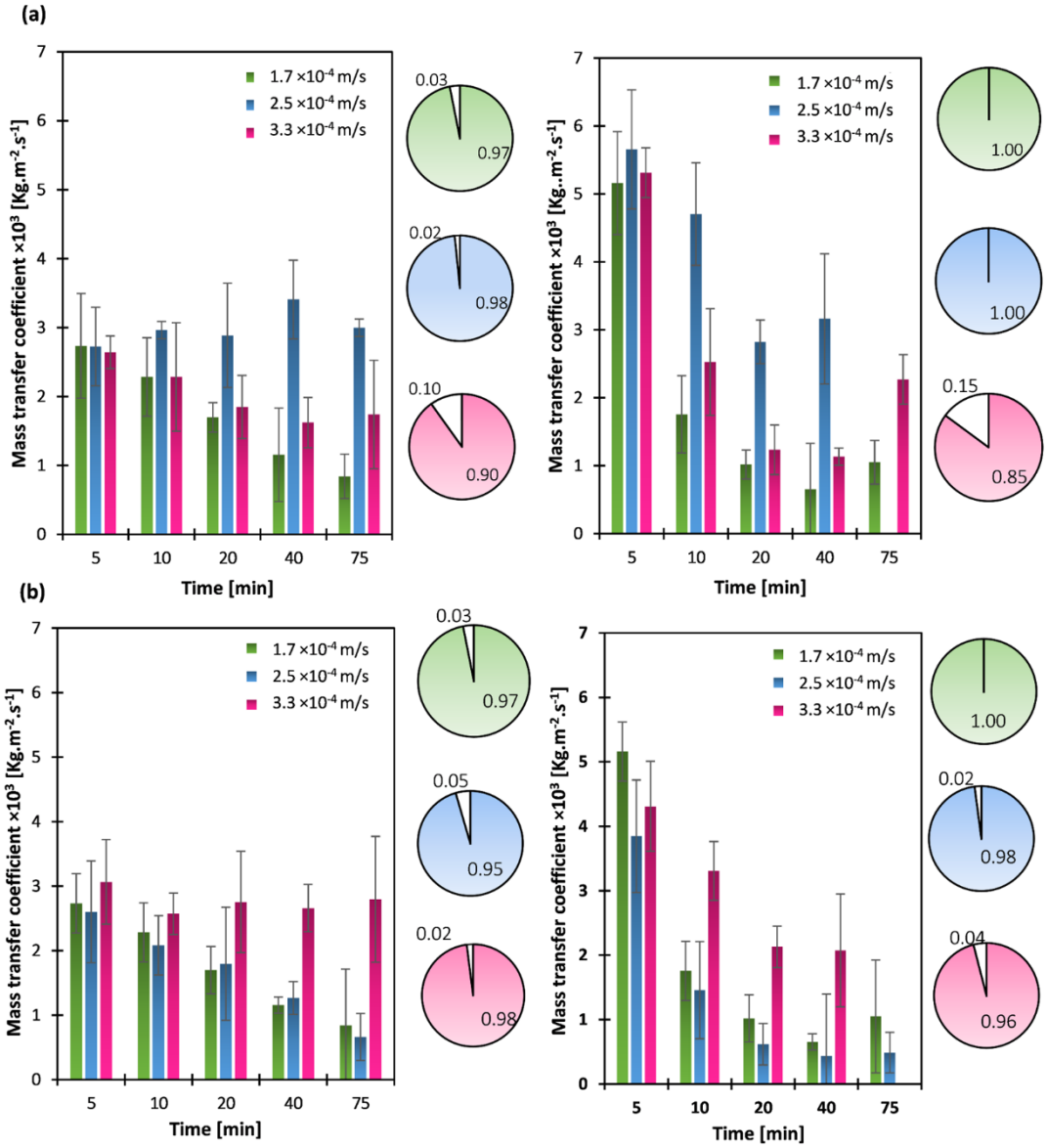

Figure 6: Mass transfer coefficient variation vis-à-vis reverse membrane permeation, i.e., permeation of water to the antisolvent side (pie charts). The pie charts represent the weight fraction of antisolvent at the end of each MAAC experiment, through PP (left) and PVDF (right) membranes, with the variation of (a) solution or (b) antisolvent velocity. A complete profile of the antisolvent composition variation with time is presented in Figure S7.

solution hydrodynamics, solution density, membrane surface roughness, etc. As far as membrane wetting is concerned, it does not necessarily cause blockage at the membrane surface. For example, in the case where the antisolvent solution velocity was set to 1.7 and 2.5 $\times 10^{-4}$ m.s^{-1} with PVDF membrane, there was no wetting detected, but the antisolvent mass transfer rate was high enough that the solution became concentrated in solid particles in a shorter time, resulting in the system blockage; notably in the membrane module or the tubing. Nonetheless, less wetting indeed allows for a more stable mass transfer coefficient with time, which explains why PP outperformed PVDF in this sense, so it is recommended to use polymers with higher hydrophobicity in this case to avoid wetting.

It is important then to rely on the mass transfer coefficient to predict the crystallization dynamics and to compare between the performance of different membranes, as it was also highlighted in other membrane-based crystallization processes.[27] The mass transfer coefficient rules out the driving force, so it reflects the true effect of the membrane itself. A steady mass transfer coefficient reflects that the membrane, given its intrinsic properties (pore size, surface roughness, tortuosity, etc.) is capable of controlling the permeation of the antisolvent resulting in uniform crystal size as it will be further demonstrated in sections 3.2 and 3.3. The comparison of the antisolvent mass transfer results with the literature is shown in Table 2.

Table 2: State of the art of membrane-assisted antisolvent crystallization. [A] stands for Antisolvent; [CS] Crystallizing solution.

Membrane description	**Crystallization system**	**Crystal properties**	**Transmembrane mass transfer**			**Ref.**
		CSD, crystal size	*Flux/ flow rate/ velocity*	*K*	*Method*	
Hydrophobic PTFE membrane, developed in lab.	[A] Ethanol; [CS] A solution of NaCl and ultrapure water.	• CV was 43.5% and average size: 41.6 µm.	-	-	J= Δm /(nπd$_0$LΔt). A balance was used to track real time mass variation. N is number of hollow fibers, d$_0$ is the fiber outer diameter and L its length.	[11]
Polyethersulfone hollow fiber membranes.	[A] Ethanol; [CS] Erythritol in water.	• CV was 50.9% and average size 50 µm.	• Flux was 1.2 – 2.8 Kg.m^{-2}.h^{-1}	-	J=ΔP.k = -D$_{AB}$ $\frac{\partial C_A}{\partial r}\Big\vert_{r=R}$, with D$_{AB}$ the diffusivity and k the mass transfer coefficient. The study explains that the overall mass transfer comprises the diffusion of the antisolvent in the membrane, then in the crystallizing solution.	[16]
Hydrophobic polypropylene hollow fiber membranes.	[A] Water and ethanol mixture with different compositions at 30 C; [CS] L-serine solution in bi-distilled water at 10 C.	-	• Flux was 1.53 or 9.1 $\times 10^{-4}$ Lh^{-1}	-	Flux was expressed as the change of solution volume over time.	[17]
Polyethersulfone hollow fiber membranes with a porosity of 0.58, assembled in lab.	[A] Ethanol; [CS] A solution of erythritol and ultrapure water.	• CV was 48% and the mean crystal size was <20 µm.	• The flux ranged between 2 and 4 Kg.m^{-2}.h^{-1}	-	J=KΔP with K the membrane permeability in [kg s^{-1} Pa^{-1}] and ΔP computed using Bernoulli's equation.	[18]
Hydrophobic Polyethylene hollow fiber membrane with a pore size of 0.1, 0.25 and 0.45 µm.	[A] Deionized water; [CS] Indomethacin in ethanol.	• Particle median diameter was 0.3 to 0.35 µm.	• Average velocity across membrane was 1.2 – 1.4 m/s	-	-	[19]

Membrane description	Crystallization system	Crystal properties	Transmembrane mass transfer			Ref.
		CSD, crystal size	*Flux/ flow rate/ velocity*	*K*	*Method*	
Porous polypropylene hollow fibers with pore size of 0.03 µm.	[A] 2-Propanol; [CS] L-asparagine in de-ionized water.	• Median crystal size was c.a. 70 µm.	• Cross flow velocity was 100 to 500 µm.s^{-1}	-	$J_{AS}= (C_{AS}/1-C_{AS}) (\dot{m}_{tot}/\rho_{AS} N\pi D_0 L)$. N is number of hollow fibers, D_0 is the fiber outer diameter, ρ_{AS} density of the antisolvent and C_{AS} its concentration measured using Gas Chromatography.	[12]
Hydrophilic Nylon-6 hollow fibers.	[A] Deionized water; [CS] Drug particles of Griseofulvin in acetone.	• Median particle size was 1.6 – 11.7 µm.	-	-	-	[20]
Polyvinylidene fluoride hollow fiber membrane.	[A] Deionized water; [CS] Griseofulvin in acetone.	• Median particle size was 93 – 95 nm.	-	-	-	[21]
Polypropylene flat sheet membranes	[A] Ethanol; [CS] Glycine in water	• CV was 50–60% • Mean particle size 23–40 µm	• Flux was 0.002–0.01 Kg/m^2.s^{-1}	-	Flux was computed based on activity difference.	[15]
Polyvinylidene fluoride and polypropylene flat sheet membranes.	[A] Ethanol; [CS] L-serine in water	• CV was 31-37 %; • Mean particle size 89-102 µm.	• Flux was 0.0002 – 0.003 Kg/m^2.s	0.0023-0.0048 kg/m^2.s	Flux was computed using equation 1 and the mass transfer coefficient using equation 2 (See section 2.2).	This study

3.2. Supersaturation

Starting with a solution concentration not far from supersaturation, drop-by-drop or batch crystallization turned the feed solution turbid within seconds, while membranes controlled the introduction of antisolvent resulting in reaching the supersaturation state within the time range of 10-20 minutes (Figure 7). Overall, PP resulted in higher supersaturation values compared to PVDF. This due to the higher amounts of the antisolvent that permeated. The low surface tension of the polypropylene could prevent the attractive forces at the membrane pores responsible for slowing down the antisolvent permeance to the crystallizing solution.

On average, high supersaturations were achieved when the crystallizing solution was set at 3.3 ×10^{-4} m.s^{-1} for both PP and PVDF membranes, likely explaining why smaller crystals were observed as in Figure 8. Strangely enough, large supersaturations were also obtained when the antisolvent solution was set at 3.3 ×10^{-4} m.s^{-1} for both PP and PVDF membranes, but this time crystals appeared slightly larger than the case were the antisolvent solution was set at 2.5 ×10^{-4} m.s^{-1}. This can be due to the partial wetting by the antisolvent when it exceeds the liquid entry pressure of the membrane pores, hence resulting in a liquid-liquid interface that promotes crystal growth.

The supersaturation rate was the most stable in the case where the antisolvent solution was set to 2.5 ×10^{-4} m.s^{-1}, while the crystallizing solution was at 1.7 ×10^{-4} m.s^{-1} for both PP and PVDF membranes. This also corresponds to the case where the transmembrane flux was slightly lower than the other cases, and the most stable. There is indeed a direct correlation between the mass transport rate through the membrane pores, and the resulting supersaturation behavior, eventually the crystal properties. Di Profio

et al., observed as well that an increase in antisolvent addition rate, increased the supersaturation rate. This was attributed to the fact that the metastable zone width enlarges when the supersaturation rate increases.[17] This also agrees with the findings of Zarkadas *et al.*, who observed that an increase in supersaturation rate resulting in a decrease of mean crystal size.[12]

It can be deduced from the supersaturation data that the induction times ranged between 20 and 40 minutes. In a previous study, we investigated the variation of induction time under different operating conditions. Induction time did not follow a clear trend with the increase or decrease of solution flow rates from either side of the membranes, but correlated directly with the transmembrane mass transfer rate such that a faster mass transfer resulted in a shorter induction time.[15]

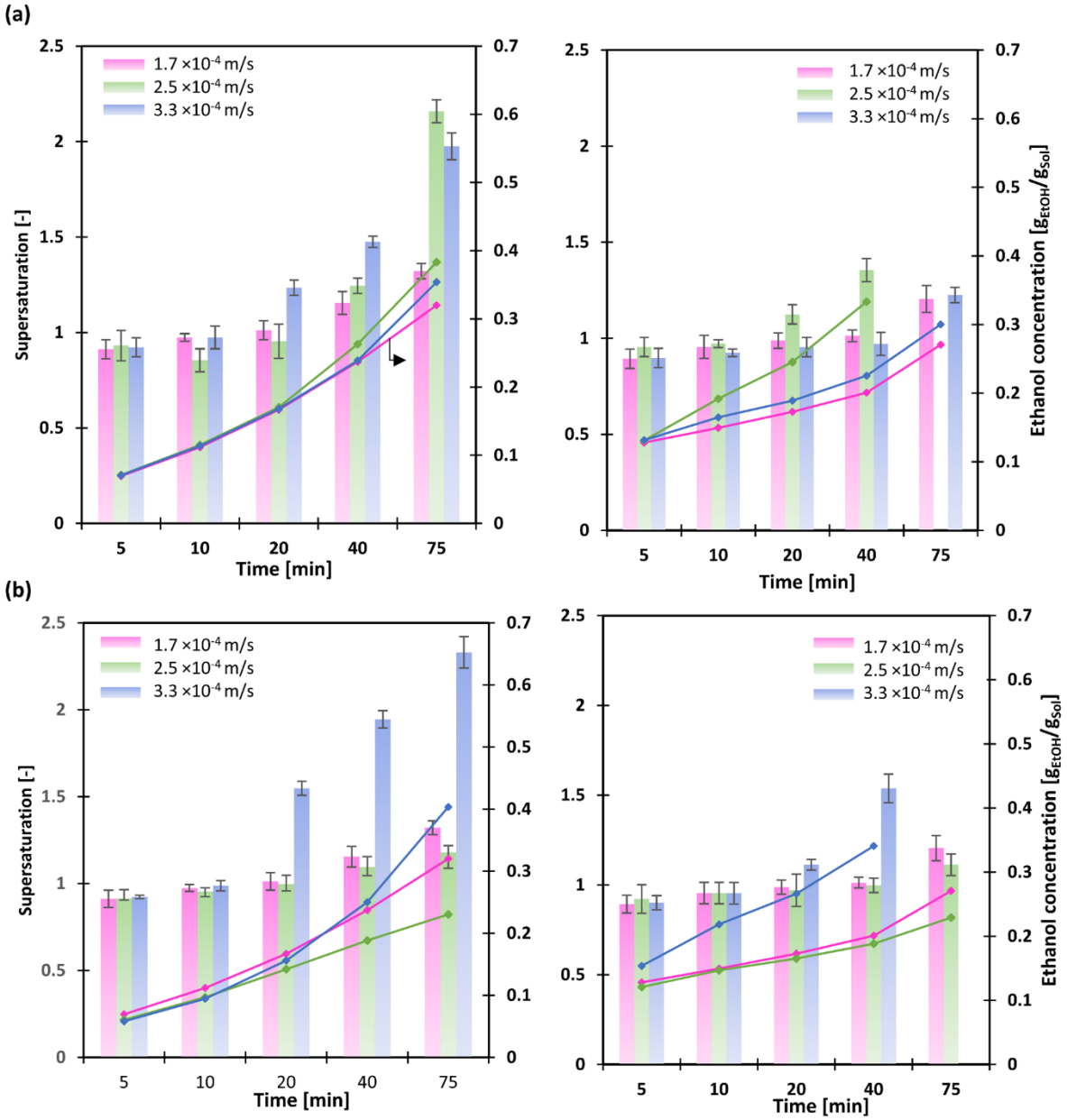

Figure 7: Supersaturation corresponding to the variation of (a) solution velocity, (b) antisolvent velocity, using PP (left) and PVDF membranes (right). The bars indicate the supersaturation, while the dots indicate weight fraction of the antisolvent ethanol as it permeates to the crystallizing solution through the membrane pores. Increase of antisolvent concentration in solution increases the supersaturation which is well controlled using membranes.

3.3. Crystal shape, crystal size distribution and crystalline system

The crystal size in all cases was around 100 µm (Figure 8), which is similar to the size of L- crystal reported by J. Luc *et al.*[28] The crystal size was the smallest in the case in which the crystallizing solution was set at 3.3×10^{-4} m/s for both PP and PVDF membranes. This is also where most partial membrane wetting took place by the crystallizing solution inducing a higher transmembrane antisolvent mass transfer and promoting more nucleation than crystal growth. On the other hand, the largest crystals were obtained in the case where the crystallizing solution was set at 2.5×10^{-4} m/s for both PP and PVDF membranes. This is also where the increase in turbulence at the crystallizing solution side promoted

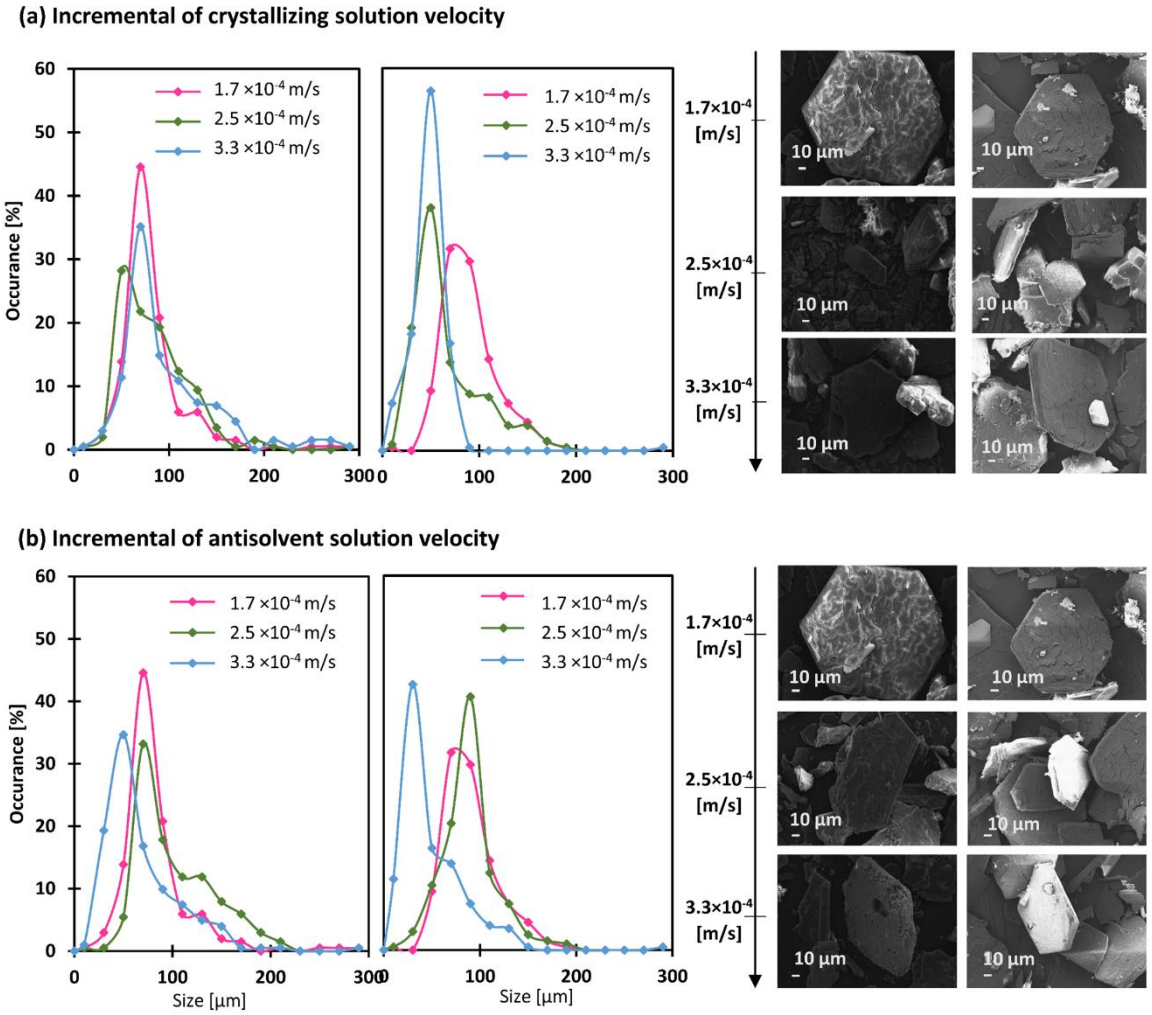

Figure 8: Crystal size distribution and crystal shape recovered from bulk solution via PP (left) and PVDF (right) membranes, with the variation of (a) crystallizing solution and (b) antisolvent velocity. SEM images of crystals recovered from the bulk demonstrated that MAAC successfully maintained the hexagonal shape of L-serine.

more mixing, a stable mass transfer and little to no apparent membrane wetting. These factors promoted more crystal growth than nucleation. These correlations between the solution velocities and crystal size was less evident from the crystals recovered from the membrane surface (Figure S8). However, the CSD was narrow at all conditions and the crystal sizes overall were larger than those recovered from the bulk solutions which is attributed to the difference in turbulence between the bulk solution and at the vicinity of the membrane.

The crystal shape in all cases consisted of hexagonal plates which corresponds to monohydrate crystals as proven previously by J. Luc *et al.*[28] It was also verified by the XRD patterns (Figure S9) that the crystalline system of the resulting crystals was orthorhombic. As far as the crystal size distribution (CSD) is concerned, MAAC successfully produced narrow size distribution (CSD) under all circumstances. This endorses the membrane's capacity to provide a one-step solution to particle formation with a narrow CSD thanks to the control of antisolvent addition.

Crystals obtained with MAAC are subject to a slow nucleation rate at the initial stage of crystallization, followed with the uniform production of fine nano-sized particles as the final product. Membranes outperformed both batch and drop-by-drop crystallization, providing a narrower CSD (Figure 9). When batch crystallization takes place, there is a burst of local nucleation that takes place before the whole solution volume gets to mix up. Similarly, with drop-by-drop crystallization, large crystals were observed to form initially with every drop before the full solution turns into a suspension of small particles. The simple mixing using the magnetic stirrer was not enough to obtain a narrow CSD; plus, the crystals were larger and did not form sharp edges, with the appearance of more agglomerates.

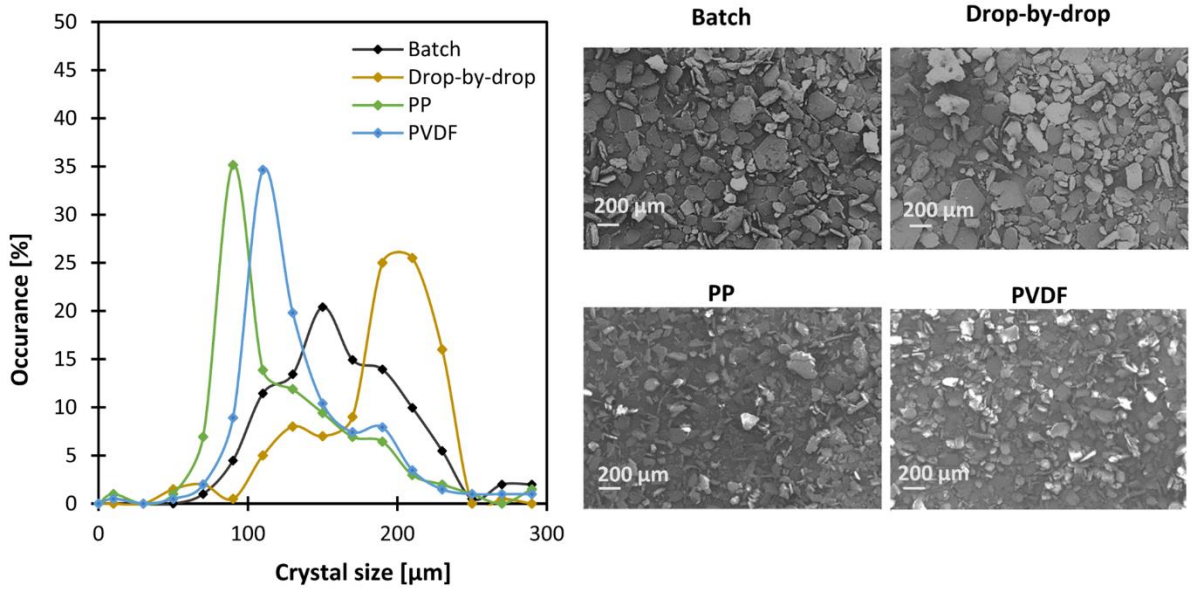

Figure 9: Comparison of CSD resulting from MAAC with drop-by-drop and batch crystallization. Samples from PVDF and PP MAAC bulk solutions at antisolvent velocity of 2.5 $\times 10^{-4}$ and feed solution velocity 1.7 $\times 10^{-4}$ m/s.

Control of crystal size and distribution is critical in the pharmaceutical industries to ensure rigorous quality requirements in the manufacturing of APIs.[29] The manufacturing of APIs involves a variety of unit operations including crystallization followed with filtration, drying and, in many cases, size reduction operations such as milling, which has a direct impact on downstream operations and end-use properties of the product.[30] The control of crystal size most importantly, helps in regulating bioavailability and absorption of poorly soluble drugs in the gastrointestinal tract.[31]

3.4. Membrane characterization before and after operation

The membrane reusability is important for future industrial applicability. To this extent, membranes were analyzed at the end of the processes. It appears from PP and PVDF cross sections (Figure 10) that traces of amino acid crystals remained at the membrane surface which resulted in the formation of small crystals of size ±20µm length. This is confirmed by the FTIR analysis (Figure 11). Furthermore, the

effect seems stronger for the PP compared to the PVDF membrane. The small peak appeared at 1580 cm^{-1} corresponds to N-H bending associated with the amine compound. As for PP, three peaks appeared at 694 and 1577 cm^{-1} correspond to C=C and N-H bending associated with alkane and amine compounds respectively. Finally, no apparent hydrophobicity change happened with PVDF maintaining a water contact angle of 130°, and a slight increase happened with PP, from 149 to 151°.

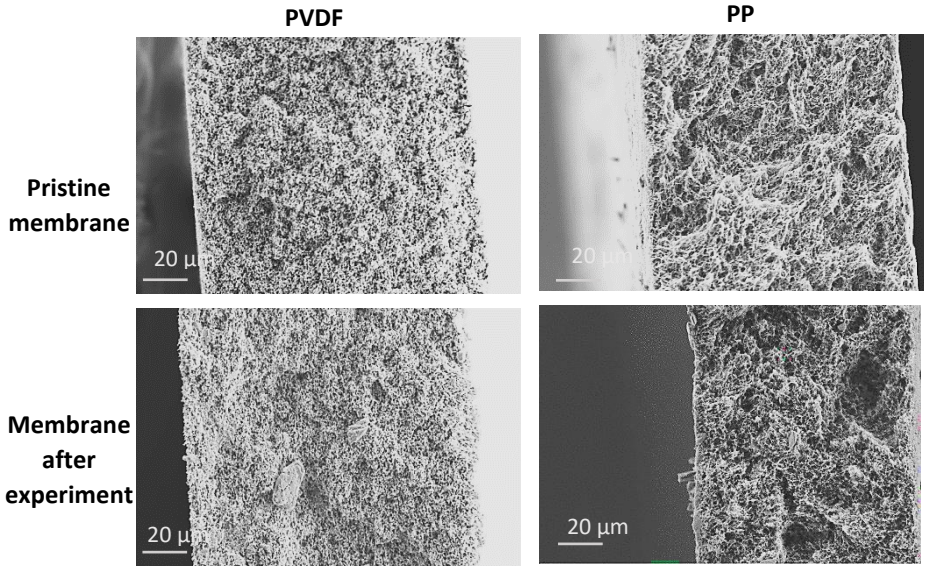

Figure 10: Cross sectional imaging of PVDF and PP membrane after MAAC experiment at antisolvent velocity of 2.5 $\times 10^{-4}$ and feed solution velocity of 1.7 $\times 10^{-4}$ m/s.

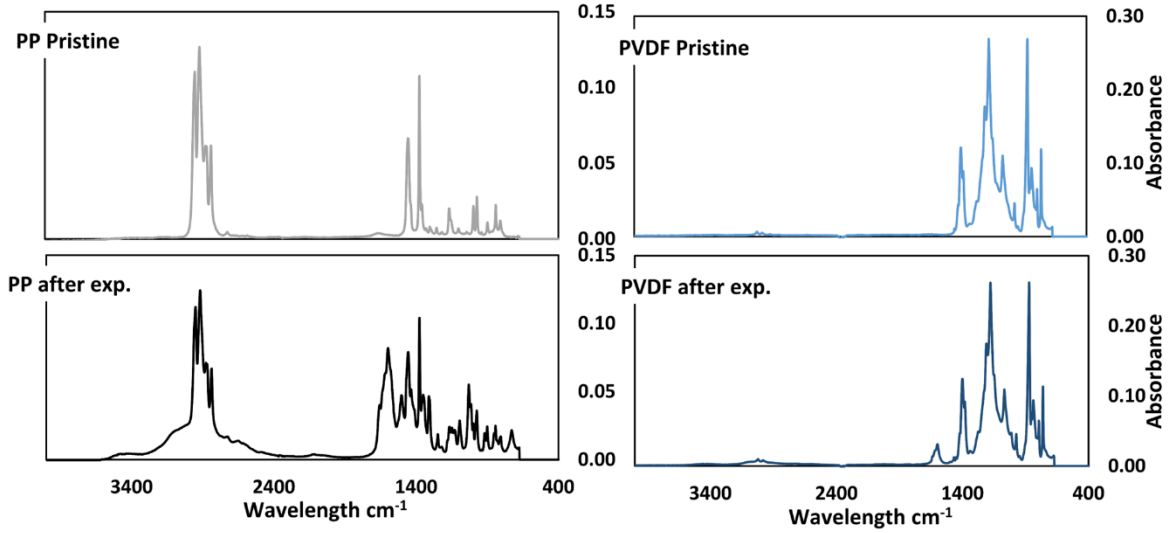

Figure 11: FTIR patterns for PVDF (left) and PP (right) membranes to evaluate any membrane surface modification after MAAC experimental. Membrane samples which were analyzed correspond to the case where antisolvent velocity of 2.5 $\times 10^{-4}$ and feed solution velocity 1.7 $\times 10^{-4}$ m/s.

Surface roughness should not have varied during MAAC operation given no significant change was observed in membrane hydrophobicity, nor in membrane morphology. Nonetheless, the membrane surface roughness is a key factor in MAAC operation yet to be thoroughly explored. Diao *et al.*, via cooling-induced crystallization, demonstrated that the pore shape of polymer films altered the nucleation

rate of aspirin.[32] Likewise, Polino *et al.*, concluded that small surface features promote nucleation due to the creation of extra nucleation sites by physical entrapment.[33] This case consisted of protein crystallization via solvent migration through the membrane. Though it was not quantified in this study, the difference in the surface roughness between PP and PVDF membranes must have played a role in controlling antisolvent crystallization, given that surface morphology in heterogeneous crystallization impacts solid-liquid phase transformation.[34]

Removal of crystal residuals from the membrane surface is necessary between MAAC operations to maintain effective membrane performance. It consists of circulating the solvent through the membrane module, in this case water for 10 to 15 minutes on both sides in the membrane module to insure no residual solutes on the membrane. Although scaling did not take place in this study, it risks decreasing the transmembrane flux using other crystallization systems. To prevent or mitigate the risk of scaling, some strategies can be adopted such as using omniphobic membranes,[35] reducing membrane surface porosity,[36] or developing preferential nucleation cites.[37] Ideally, once the nuclei are formed, they detach from the membrane surface with the help of shear stress induced at the membrane surface by the flow dynamics.

4. Conclusion

This study demonstrated the role of membranes in controlling antisolvent crystallization via investigating the transmembrane mass transfer and its correlation with the crystal characteristics, notably, the crystal size distribution and shape.

Polyvinylidene fluoride (PVDF) and polypropylene (PP) commercial membranes were evaluated in their MAAC performance and they both showed superior performance with the crystal size coefficient of variation (CV) within 31-37% compared with batch antisolvent crystallization and drop-by-drop where CV equaled 54 and 63% respectively. This is due to the efficient mixing that is provided by the membranes where the antisolvent permeates through the pores, giving multiple points of diffusion between the antisolvent and the crystallizing solution, making is smoother for the solid-liquid interface to take place for crystallization.

A closer look at the antisolvent transmembrane mass transfer through the membrane showed that the velocity at which the crystallizing or the antisolvent solution is circulating plays a role in the variation of the antisolvent transmembrane flux and membrane wetting. This correlates directly with the final crystal size distribution:

(i) The transmembrane flux of the antisolvent through PP membranes continued to flow for 75 minutes, while using PVDF membranes faced system blockage at 40 minutes in two scenarios, in case where the crystallizing solution was set at 2.5×10^{-4} m/s and where the antisolvent was set at 3.3×10^{-4} m/s. This was explained by the higher crystal growth resulting from a higher mass transfer rate of the antisolvent.

(ii) Neither membrane have endured any major change after MAAC operation, although slightly more nano-crystals appeared at the cross section of PP compared to PVDF membranes, as well as more functional groups appeared on PP surfaces which could have slightly altered the interaction between the membrane and crystallizing solution.

In all, both membranes are recommended to perform MAAC, under optimum conditions such as solution velocity. PP membrane gave better control of the antisolvent mass transfer mainly given its lower surface tension, while the membrane pore size and cross-sectional structure were the same in both PP and PVDF

membranes. These findings are of pertinent interest to produce crystalline pharmaceutical compounds avoiding cumbersome downstream processing.

Associated content

Figure S1: Real image of experimental set up; Figure S2: Ethanol activity coefficient variation; Figure S3: HPLC calibration curve for the quantitative analysis of L-serine content; Figure S4: GC calibration curve for the quantitative analysis of ethanol content; Figure S5: Solubility curve of L-serine in water-ethanol solution mixture; Figure S6: Evolution of L-serine crystal morphology with increase of antisolvent concentration in the crystallization solution; Figure S7: Concentration of ethanol in the antisolvent solution with time of antisolvent through PP and PVDF membranes; Figure S8: Crystal size distribution and SEM images of crystals recovered from the membrane surface; Figure S9: XRD patterns illustrating that both PVDF and PP result in L-serine crystals with orthorhombic crystal structure.

Author information

Corresponding authors: Sara Chergaoui—Email: sara.chergaoui@uclouvain.be; Patricia Luis—Email: patricia.luis@uclouvain.be

Author contributions: Conceptualization, S.C. and P.L.; methodology, S.C. and P.L.; validation, T.L., D.P.D. and P.L.; formal analysis, S.C.; investigation, S.C.; writing—original draft preparation, S.C.; visualization, S.C.; supervision, P.L.; project administration, T.L., D.P.D. and P.L.; funding acquisition, T.L., D.P.D. and P.L. The authors declare no competing financial interest.

Acknowledgements

This work has been funded by Actions de Recherche Concerté (ARC) under the project PURE-20/25-108—New approaches in Process Intensification: Towards combined PUrefication-REaction Membrane based processes.

References

(1) Testa, C. J.; Shvedova, K.; Hu, C.; Wu, W.; Born, S. C.; Takizawa, B.; Mascia, S. Heterogeneous Crystallization as a Process Intensification Technology in an Integrated Continuous Manufacturing Process for Pharmaceuticals. *Org. Process Res. Dev.* **2021**, *25* (2), 225–238. https://doi.org/10.1021/acs.oprd.0c00468.

(2) Ostergaard, I.; Szilagyi, B.; de Diego, H. L.; Qu, H.; Nagy, Z. K. Polymorphic Control and Scale-Up Strategy for Antisolvent Crystallization Using Direct Nucleation Control. *Cryst. Growth Des.* **2020**, *20* (4), 2683–2697. https://doi.org/10.1021/acs.cgd.0c00101.

(3) Duffy, D.; Barrett, M.; Glennon, B. Novel, Calibration-Free Strategies for Supersaturation Control in Antisolvent Crystallization Processes. *Cryst. Growth Des.* **2013**, *13* (8), 3321–3332. https://doi.org/10.1021/cg301673g.

(4) Zhou, G. X.; Fujiwara, M.; Woo, X. Y.; Rusli, E.; Tung, H.-H.; Starbuck, C.; Davidson, O.; Ge, Z.; Braatz, R. D. Direct Design of Pharmaceutical Antisolvent Crystallization through Concentration Control. *Cryst. Growth Des.* **2006**, *6* (4), 892–898. https://doi.org/10.1021/cg0504049.

(5) *Crystallization Technology Handbook*, 2nd ed., rev.expanded.; Mersmann, A., Ed.; Marcel Dekker: New York, 2001.

(6) Nagy, Z. K.; Fujiwara, M.; Braatz, R. D. Modelling and Control of Combined Cooling and Antisolvent Crystallization Processes. *J. Process Control* **2008**, *18* (9), 856–864. https://doi.org/10.1016/j.jprocont.2008.06.002.

(7) Yan, Z.; Lu, Z.; Chen, X.; Fan, G.; Qu, F.; Pang, H.; Liang, H. Integration of Seeding- and Heating-Induced Crystallization with Membrane Distillation for Membrane Gypsum Scaling and Wetting Control. *Desalination* **2021**, *511*, 115115. https://doi.org/10.1016/j.desal.2021.115115.

(8) Nagy, Z. K.; Fujiwara, M.; Braatz, R. D. Modelling and Control of Combined Cooling and Antisolvent Crystallization Processes. *J. Process Control* **2008**, *18* (9), 856–864. https://doi.org/10.1016/j.jprocont.2008.06.002.

(9) Wu, B.; Li, J.; Li, C.; He, J.; Luo, P. Antisolvent Crystallization Intensified by a Jet Crystallizer and a Method for Investigating Crystallization Kinetics. *Chem. Eng. Sci.* **2020**, *211*, 115259. https://doi.org/10.1016/j.ces.2019.115259.

(10) Sparenberg, M.-C.; Chergaoui, S.; Sang Sefidi, V.; Luis, P. Crystallization Control via Membrane Distillation-Crystallization: A Review. *Desalination* **2021**, *519*, 115315. https://doi.org/10.1016/j.desal.2021.115315.

(11) Sheng, L.; Li, J.; He, G.; Xiao, W.; Yan, X.; Li, X.; Ruan, X.; Jiang, X. Visual Study and Simulation of Interfacial Liquid Layer Mass Transfer in Membrane-Assisted Antisolvent Crystallization. *Chem. Eng. Sci.* **2020**, *228*, 116003. https://doi.org/10.1016/j.ces.2020.116003.

(12) Zarkadas, D. M.; Sirkar, K. K. Antisolvent Crystallization in Porous Hollow Fiber Devices. *Chem. Eng. Sci.* **2006**, *61* (15), 5030–5048. https://doi.org/10.1016/j.ces.2006.03.036.

(13) Curcio, E.; Di Profio, G. CHAPTER 8. Continuous Membrane Crystallization. In *The Handbook of Continuous Crystallization*; Yazdanpanah, N., Nagy, Z. K., Eds.; Royal Society of Chemistry: Cambridge, 2020; pp 321–352. https://doi.org/10.1039/9781788013581-00321.

(14) Jiang, X.; Shao, Y.; Sheng, L.; Li, P.; He, G. Membrane Crystallization for Process Intensification and Control: A Review. *Engineering* **2020**, S2095809920303611. https://doi.org/10.1016/j.eng.2020.06.024.

(15) Chergaoui, S.; Debecker, D. P.; Leyssens, T.; Luis, P. Key Parameters Impacting the Crystal Formation in Antisolvent Membrane-Assisted Crystallization. *Membranes* **2023**, *13* (2), 140. https://doi.org/10.3390/membranes13020140.

(16) Li, J.; Sheng, L.; Tuo, L.; Xiao, W.; Ruan, X.; Yan, X.; He, G.; Jiang, X. Membrane-Assisted Antisolvent Crystallization: Interfacial Mass-Transfer Simulation and Multistage Process Control. *Ind. Eng. Chem. Res.* **2020**, *59* (21), 10160–10171. https://doi.org/10.1021/acs.iecr.0c01645.

(17) Di Profio, G.; Stabile, C.; Caridi, A.; Curcio, E.; Drioli, E. Antisolvent Membrane Crystallization of Pharmaceutical Compounds. *J. Pharm. Sci.* **2009**, *98* (12), 4902–4913. https://doi.org/10.1002/jps.21785.

(18) Tuo, L.; Ruan, X.; Xiao, W.; Li, X.; He, G.; Jiang, X. A Novel Hollow Fiber Membrane-Assisted Antisolvent Crystallization for Enhanced Mass Transfer Process Control. *AIChE J.* **2019**, *65* (2), 734–744. https://doi.org/10.1002/aic.16438.

(19) Fern, J. C. W.; Ohsaki, S.; Watano, S.; Pfeffer, R. Continuous Synthesis of Nano-Drug Particles by Antisolvent Crystallization Using a Porous Hollow-Fiber Membrane Module. *Int. J. Pharm.* **2018**, *543* (1–2), 139–150. https://doi.org/10.1016/j.ijpharm.2018.03.025.

(20) Chen, D.; Singh, D.; Sirkar, K. K.; Pfeffer, R. Continuous Synthesis of Polymer-Coated Drug Particles by Porous Hollow Fiber Membrane-Based Antisolvent Crystallization. *Langmuir* **2015**, *31* (1), 432–441. https://doi.org/10.1021/la503179t.

(21) Zhou, X.; Wang, B.; Liu, Q.; Liu, C.; Gao, X.; Sirkar, K. K.; Chen, D. An Extended Duration Operation for Porous Hollow Fiber-Based Antisolvent Crystallization. *Ind. Eng. Chem. Res.* **2019**, *58* (27), 12431–12437. https://doi.org/10.1021/acs.iecr.9b02028.

(22) Servi, A. T.; Kharraz, J.; Klee, D.; Notarangelo, K.; Eyob, B.; Guillen-Burrieza, E.; Liu, A.; Arafat, H. A.; Gleason, K. K. A Systematic Study of the Impact of Hydrophobicity on the Wetting of MD Membranes. *J. Membr. Sci.* **2016**, *520*, 850–859. https://doi.org/10.1016/j.memsci.2016.08.021.

(23) Roelands, C. P. M.; Jiang, S.; Kitamura, M.; Kramer, H. J. M.; Jansens, P. J. Antisolvent Crystallization of the Polymorphs of L-Histidine as a Function of Supersaturation Ratio and of Solvent Composition. 9.

(24) Mohammad, A. W.; Ng, C. Y.; Lim, Y. P.; Ng, G. H. Ultrafiltration in Food Processing Industry: Review on Application, Membrane Fouling, and Fouling Control. *Food Bioprocess Technol.* **2012**, *5* (4), 1143–1156. https://doi.org/10.1007/s11947-012-0806-9.

(25) Ong, Y. K.; Widjojo, N.; Chung, T.-S. Fundamentals of Semi-Crystalline Poly(Vinylidene Fluoride) Membrane Formation and Its Prospects for Biofuel (Ethanol and Acetone) Separation via Pervaporation. *J. Membr. Sci.* **2011**, *378* (1–2), 149–162. https://doi.org/10.1016/j.memsci.2011.04.037.

(26) Tsampanakis, I.; Orbaek White, A. The Mechanics of Forming Ideal Polymer–Solvent Combinations for Open-Loop Chemical Recycling of Solvents and Plastics. *Polymers* **2021**, *14* (1), 112. https://doi.org/10.3390/polym14010112.

(27) Sparenberg, M.-C.; Hanot, B.; Molina-Fernández, C.; Luis, P. Experimental Mass Transfer Comparison between Vacuum and Direct Contact Membrane Distillation for the Concentration of Carbonate Solutions. *Sep. Purif. Technol.* **2021**, *275*, 119193. https://doi.org/10.1016/j.seppur.2021.119193.

(28) Luk, C. J.; Rousseau, R. W. Solubilities of and Transformations between the Anhydrous and Hydrated Forms of L -Serine in Water−Methanol Solutions. *Cryst. Growth Des.* **2006**, *6* (8), 1808–1812. https://doi.org/10.1021/cg0601204.

(29) Eren, A.; Szilagyi, B.; Quon, J. L.; Papageorgiou, C. D.; Nagy, Z. K. Experimental Investigation of an Integrated Crystallization and Wet-Milling System with Temperature Cycling to Control the Size and Aspect Ratio of Needle-Shaped Pharmaceutical Crystals. *Cryst. Growth Des.* **2021**, *21* (7), 3981–3993. https://doi.org/10.1021/acs.cgd.1c00308.

(30) Cruz, P.; Alvarez, C.; Rocha, F.; Ferreira, A. Tailoring the Crystal Size Distribution of an Active Pharmaceutical Ingredient by Continuous Antisolvent Crystallization in a Planar Oscillatory Flow Crystallizer. *Chem. Eng. Res. Des.* **2021**, *175*, 115–123. https://doi.org/10.1016/j.cherd.2021.08.030.

(31) Khan, K. U.; Minhas, M. U.; Badshah, S. F.; Suhail, M.; Ahmad, A.; Ijaz, S. Overview of Nanoparticulate Strategies for Solubility Enhancement of Poorly Soluble Drugs. *Life Sci.* **2022**, *291*, 120301. https://doi.org/10.1016/j.lfs.2022.120301.

(32) Diao, Y.; Harada, T.; Myerson, A. S.; Alan Hatton, T.; Trout, B. L. The Role of Nanopore Shape in Surface-Induced Crystallization. *Nat. Mater.* **2011**, *10* (11), 867–871. https://doi.org/10.1038/nmat3117.

(33) Polino, M.; Portugal, C. A. M.; Le The, H.; Tiggelaar, R.; Eijkel, J.; Crespo, J. G.; Coelhoso, I. M.; Pina, M. P.; Mallada, R. Enhanced Protein Crystallization on Nafion Membranes Modified by Low-Cost Surface Patterning Techniques. *Cryst. Growth Des.* **2020**, *20* (4), 2174–2186. https://doi.org/10.1021/acs.cgd.9b00969.

(34) Diao, Y.; Myerson, A. S.; Hatton, T. A.; Trout, B. L. Surface Design for Controlled Crystallization: The Role of Surface Chemistry and Nanoscale Pores in Heterogeneous Nucleation. *Langmuir* **2011**, *27* (9), 5324–5334. https://doi.org/10.1021/la104351k.

(35) Pan, T.; Liu, J.; Deng, N.; Li, Z.; Wang, L.; Xia, Z.; Fan, J.; Liu, Y. ZnO Nanowires@PVDF Nanofiber Membrane with Superhydrophobicity for Enhanced Anti-Wetting and Anti-Scaling Properties in Membrane Distillation. *J. Membr. Sci.* **2021**, *621*, 118877. https://doi.org/10.1016/j.memsci.2020.118877.

(36) Liu, L.; Xiao, Z.; Liu, Y.; Li, X.; Yin, H.; Volkov, A.; He, T. Understanding the Fouling/Scaling Resistance of Superhydrophobic/Omniphobic Membranes in Membrane Distillation. *Desalination* **2021**, *499*, 114864. https://doi.org/10.1016/j.desal.2020.114864.

(37) Polino, M.; Portugal, C. A. M.; Di Profio, G.; Coelhoso, I. M.; Crespo, J. G. Protein Crystallization by Membrane-Assisted Technology. *Cryst. Growth Des.* **2019**, *19* (8), 4871–4883. https://doi.org/10.1021/acs.cgd.9b00223.

For Table of Contents Use Only

Manuscript title

Control of antisolvent mass transfer through porous membranes for the crystallization of organic compounds

Authors list

Sara Chergaoui[1,2*], Damien P. Debecker[2,3], Tom Leyssens[2,3], Patricia Luis[1,2*]

[1] Institute of Mechanics, Materials and Civil Engineering - Materials & Process Engineering (iMMC-IMAP), Université catholique de Louvain (UCLouvain), Place Sainte Barbe, 2 bte L5.02.02-B, 1348 Louvain-la-Neuve, Belgium

[2] Research & Innovation Centre for Process Engineering (ReCIPE), Université catholique de Louvain (UCLouvain), Place Sainte Barbe, 2 bte L5.02.02-B, 1348 Louvain-la-Neuve, Belgium

[3] Institute of Condensed Matter and Nanosciences (IMCN), Université catholique de Louvain (UCLouvain), Place Louis Pasteur, 1 bte L4.01.06, 1348 Louvain-la-Neuve, Belgium

TOC graphic

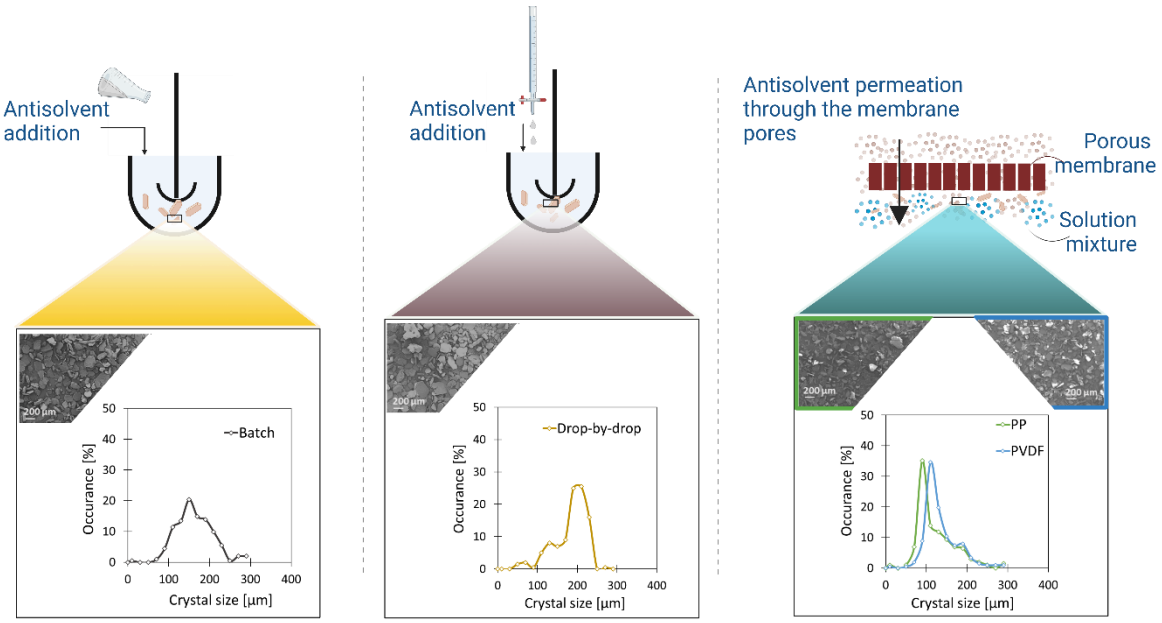

Synopsis

Membrane-assisted antisolvent crystallization (MAAC) is investigated through the evaluation of the transmembrane mass transfer, the evolution of supersaturation and its impact on crystal size and size distribution. L-serine in water was chosen as the crystallization system with ethanol as antisolvent. Some potential challenges in MAAC operation were also addressed and their mitigation pathways.